# LOGSAGE: LOG-BASED SALIENCY FOR GUIDED ENCODING IN ROBUST NUCLEI SEGMENTATION OF IMMUNOFLUORESCENCE HISTOLOGY IMAGES

*Sahar A Mohammed[1], Siyavash Shabani[1], Muhammad Sohaib[1], Corina Nicolescu[1], Mary Helen Barcellos-Hoff[2], and Bahram Parvin[1,3,4,*]*

[1] Department of Electrical and Biomedical Engineering, University of Nevada, Reno (UNR)
[2] Department of Radiation Oncology, University of California, San Francisco
[3] Pennington Cancer Institute
[4] Department of Microbiology and Immunology, College of Medicine, (UNR)

2025 IEEE 22nd International Symposium on Biomedical Imaging (ISBI) | 979-8-3315-2052-6/25/$31.00 ©2025 IEEE | DOI: 10.1109/ISBI60581.2025.10980672

**ABSTRACT**

The tumor microenvironment (TME) is critical in cancer progression, development, and treatment response. However, its complex cellular architecture (e.g., cell type, organization) presents significant challenges for accurate immunofluorescence (IF) image segmentation. We introduce the **LoGSAGE** (**LoG**-based **SA**liency for **G**uided **E**ncoding) model, which couples a Swin Transformer with the encoded response from Laplacian of Gaussian (LoG) on multiple scales. The loss function incorporates two deformation metrics, combining the Dice- and curvature alignment loss. The model is applied to a large cohort of preclinical data and has shown an improved performance over the state-of-the-art methods. The proposed model achieved a Dice score of 94.92% and a Panoptic Quality (PQ) score of 81%. This model supports robust profiling of the TME for sensitive assays.

***Index Terms***— Tumor Microenvironment, Nuclear Segmentation, Immunofluorescence Imaging, Swin Transformer, Laplacian of Gaussian, Curvature Loss

## 1. INTRODUCTION

The TME is critical in tumor progression and treatment outcomes, making it a central focus in cancer research. Detailed characterization of immune-related features within the TME has enhanced our understanding of immunoregulation in cancer, revealing how these characteristics influence responses to immunotherapy [1]. However, the dense nuclear packing and structural complexity in IF tissue sections present segmentation challenges that many existing methods, such as SAM [2], CellVit [3], Cellpose [4], and Stardist [5], often struggle to overcome. While annotated datasets exist for H&E and IHC images, comparable resources for IF tissue sections are limited, underscoring the need for tailored segmentation methods [6].

Numerous advancements in nuclear segmentation methods have been documented in recent years [7], [8], [9], [10], covering both 2D and 3D segmentation across various staining modalities. The UNet architecture [11] and its variants, SharpBlock UNet [12] and AL-net [13], are central to nuclear segmentation due to their robustness in handling complex tasks like distinguishing each nucleus in densely packed cellular organization. These architectures have demonstrated strong performance across various segmentation challenges, making them key contributors to advancements in this area. For example, StarDist innovates by predicting star-convex polygons, enhancing precision in challenging scenarios [5]. CellPose adapts UNet to predict vector fields for robust segmentation across different microscopy modalities [4].

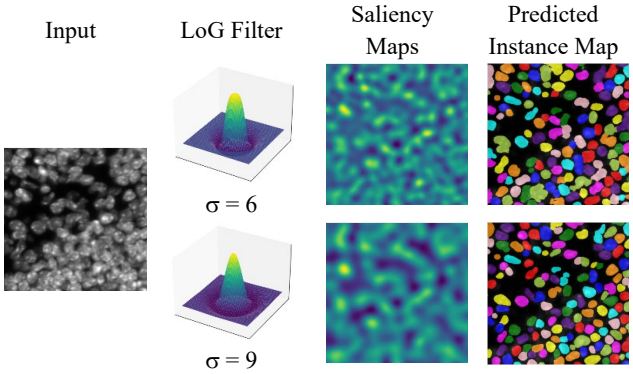


**Fig. 1.** The LoG responses (σ = 6 and σ = 9) generate saliency maps to improve nuclei segmentation.

Additionally, integrated systems like CellViT [3], and Hover-Net [14] Combine segmentation with classification by leveraging transformer architectures alongside convolutional layers, offering comprehensive solutions for complex segmentation tasks. These advancements are complemented with modified loss functions such as (a) integrating principal component analysis for anatomical accuracy [15], (b) distance transform or Hausdorff distance for emphasizing perceptual boundaries for segmenting a clump of nuclei [16], [17], [18], (c) coupling detection and segmentation, including loss associated with the bounding box in CellSeg [19], and

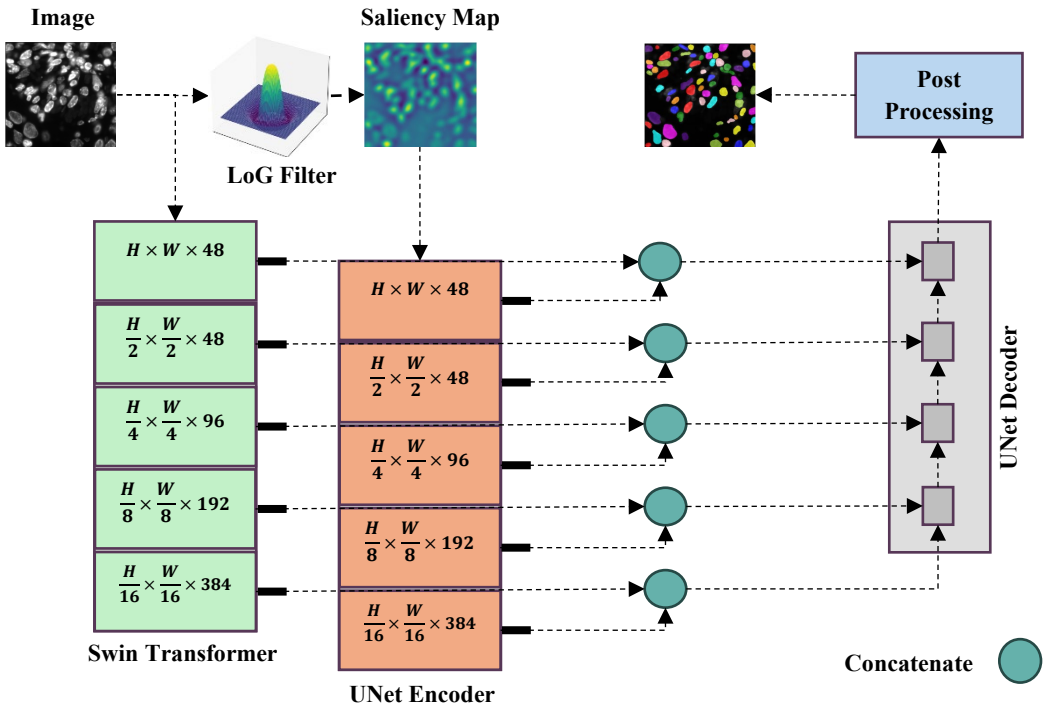


**Fig. 2.** Model architecture incorporates the LoG response as a saliency map in combination with the Swin Transformer.

(d) boundary mining loss as demonstrated in BoNuS that uses multiple-instance learning coupled with boundary information through pixel affinities [20]. In recent years, development in large language models has led to the Segment Anything Model (SAM) [2], which provides adequate results for further fine-tuning. However, SAM has a heavy footprint and is not optimized for specialization.

Our computational pipeline targets a biobank of in-house mammary tumors in a preclinical model. Each histology section is stained with multiple markers to investigate the role of inflammation in tumor development. A foundational step is the robust delineation of nuclei within the TME, enabling cell-by-cell measurements that construct organizational and functional maps for each histology section. While we initially evaluated state-of-the-art (SOTA) segmentation models on this complex dataset, their performance fell short, motivating the development of a custom model to address our specific challenges.

Our approach is inspired by the framework from *Transformers Pay Attention to Convolutions* [21], which enhances skip connections through attention maps generated by *DINO* [22]. We integrate outputs from a Swin Transformer, leveraging its hierarchical architecture for global and local feature extraction. Swin Transformers perform well in both 2D [23] and 3D configurations [24], [25], effectively addressing the structural complexity of the TME. These outputs are combined with those from a UNet-based encoder that processes saliency maps derived from Laplacian of Gaussian (LoG) responses. Figure 1 shows examples of these saliency maps generated at different sigma values, illustrating how LoG-filtered maps highlight nuclear regions, and supporting a more accurate segmentation. The combined outputs are then processed through a UNet-based decoder for segmentation. This fusion of spatial features with intrinsic saliency enhances nuclei segmentation by leveraging positional and contextual information. While this approach significantly improves segmentation, further refinement is needed to partition clustered nuclei accurately. To address this, we implemented a custom loss function incorporating curvature along object contours, promoting accurate delineation of individual nuclei within densely packed regions while preserving localized structure. This combination of architectural design and custom loss function provides robust segmentation, which is critical for TME profiling in tissue histology.

The manuscript is organized as follows: Section 2 describes the methodology, Section 3 presents and interprets the results, and Section 4 concludes the paper.

## 2. METHOD

### 2.1 Data Preparation

We manually annotated each nucleus using QuPath [26] and applied one-pixel erosion to enhance separation, partitioning images into 256×256-pixel patches. To increase variability and robustness, we applied Annotation, followed by data augmentation that includes flipping, rotation, scaling, and intensity adjustments. The latter can provide a rich diversity of cellular states that mimic the continuum in the cell cycle.

### 2.2 Model Architecture

LoGSAGE, shown in Figure 2, combines a Swin Transformer and a UNet-based saliency encoder. The Swin Transformer extracts multi-scale features from the input image using window-based self-attention, while the UNet encoder

processes LoG-filtered saliency maps. Features from both encoders are fused at each scale and passed through a UNet decoder with up-convolutions and concatenations, refining the segmentation at each stage. A final 1x1 convolution generates the segmentation map.

### 2.3 Loss Function

Since overlapping or touching nuclei can present challenges in segmentation, we introduce Curvature Alignment Loss (CAL) to help separate closely positioned nuclei in combination with the Dice loss.

**Curvature Alignment Loss (CAL):** This term computes curvature along contours in the predicted and ground truth, comparing their distributions via KL divergence. Curvature κ is calculated using derivatives measured with a Gaussian filter (σ, window size 9σ) applied to contour coordinates, defined as:

$$\kappa = \frac{dx.ddy - dy.ddx}{(dx^2 + dy^2)^{3/2}} \quad (1)$$

where $(dx)$ and $(dy)$ Are the first derivatives, and $(ddx)$ and $(ddy)$ Are the second derivatives, both measured with a Gaussian kernel $(\sigma)$ Controls the scale of curvature details, balancing fine and coarse boundary features.

**Curvature Distributions and KL Divergence:** We compute the probability density functions (PDFs) of curvature values for predicted and ground truth contours. The curvature loss is then calculated as the KL Divergence between the two PDFs:

$$CAL = \sum_{x \in X} PDF_{Curv\_pred}(x) \log\left(\frac{PDF_{Curv\_pred}(x)}{PDF_{Curv\_GT}(x)}\right) \quad (2)$$

Our total Custom Loss Function (CLF) is defined as:

$$CLF = \alpha \times DL + \beta \times \mathrm{CAL} \quad (3)$$

Where α, and β are hyperparameters optimized based on simulation studies.

Figure 3 illustrates the curvature along the contours of ground truth and predicted segmentation during training, highlighting areas with maximum curvature in red.

### 2.4 Training and Inference

The model was trained using the Adam optimizer with a batch size 20, batch normalization, dropout, weight decay, and a learning rate scheduler to minimize a combined loss. The training data was split 80/20 for training and validation, with the Dice score calculated per epoch. The best model state was saved based on improvements in validation loss. The training utilized the DAPI channel and LoG response images as inputs. Hyperparameter tuning targeted the Curvature Alignment Loss (CAL) weight, calibrated from 0 (alignment) to 1 (misalignment), with a search around values of 0.1, 0.3, 0.5, 0.7, and 1. To verify that training data composition did not influence downstream analyses, we expanded the training set from 6 images (yielding 2,268 augmented patches) to 8 images (3,024 samples). The Dice score remained stable with this increase, indicating that dataset size had no significant impact on biological analysis outcomes and affirming the model's robustness to variations in training set size.

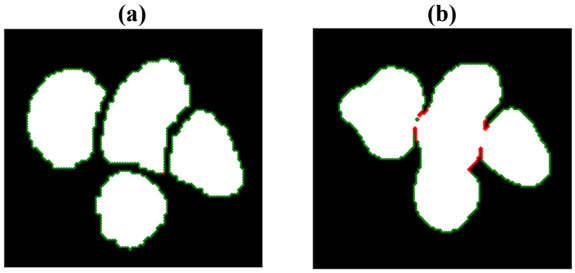


**Fig. 3:** Curvature along the contours of (a) ground truth and (b) predicted segmentation is visualized, with red indicating regions of high curvature associated with high loss values.

## 3. RESULTS AND DISCUSSION

The model's performance was evaluated exclusively on a curated dataset of mouse mammary gland tumors, integral to our computational pipeline. This dataset enables a comprehensive assessment of segmentation accuracy within complex TMEs, supporting the model's reliability in intricate biological contexts.

As an initial step, we evaluated the performance of standard State-of-the-Art (SOTA) segmentation models on our dataset. While the pre-trained models demonstrated reasonable performance, their retrained versions using our annotated dataset showed only marginal improvements for most methods. However, the UNet and Swin Transformer, trained from scratch, performed notably better than the other models, as summarized in Table 1. Nevertheless, we used them as baseline models for our proposed approach.

| Model | Pretrain | | Trained | |
|---|---|---|---|---|
| | Avg. Dice | Avg. PQ | Avg. Dice | Avg.PQ |
| StarDist | 80.4 | 60.46 | 86.5 | 63.56 |
| CellPose | 77.1 | 59.86 | 85.8 | 64.66 |
| SAM | 85.5 | 64.58 | 87.2 | 65.23 |
| CellViT | - | - | 89.0 | 69.03 |
| **UNet*** | **-** | **-** | 90.41 | **76.78** |
| **SwinT*** | **-** | **-** | **91.67** | 72.17 |

**Table 1**: The Dice and PQ scores of the SOTA segmentation models are compared with and without training on our datasets. UNet and Swin Transformer were trained from scratch.

We evaluated segmentation performance across varying sigma values in the LoG filter (4–10) and compared it with the performance of the Swin Transformer alone.

As shown in Table 2, segmentation results were relatively consistent across sigma values, with sigma=9 achieving the highest Dice score and slightly outperforming other settings. The standalone Swin Transformer (Table 1), trained from scratch, yielded lower accuracy, indicating that optimized LoG filtering enhances segmentation performance.

| Sigma ( $\sigma$) | Avg. Dice | Avg. PQ |
|---|---|---|
| 4 | 93.01 ± 0.2 | 76.53 |
| 5 | 93.02 ± 0.2 | 76.96 |
| 6 | 92.96 ± 0.3 | 69.06 |
| 7 | 93.11 ± 0.1 | 77.50 |
| 8 | 93.33 ± 0.1 | 77.67 |
| **9** | **93.49 ± 0.1** | **77.92** |
| 10 | 93.39 ± 0.1 | 77.79 |

**Table 2:** The ablation study compares the performance of LoGSAGE at different scales using 3-fold cross-validation.

To assess the impact of the Curvature Alignment Loss (CAL) weight on segmentation performance, we performed a hyperparameter search with different CAL weights (0.1, 0.3, 0.5, 0.7, and 1). As shown in Table 3, the Dice score varied slightly across these weights, with a CAL weight of 0.5, achieving the highest score (94.92). This result suggests that a moderate CAL weight optimizes segmentation, as both lower (0.1) and higher (1) values yielded slightly reduced Performance (91.62 and 89.78, respectively).

| CAL weight (β) | Avg. Dice | Avg. PQ |
|---|---|---|
| 0.1 | 91.62 ± 0.2 | 72.01 |
| 0.3 | 92.62 ± 0.3 | 68.75 |
| **0.5** | **94.92 ± 0.3** | **81.00** |
| 0.7 | 93.37 ± 0.2 | 77.69 |
| 1 | 89.78 ± 0.1 | 71.13 |

**Table 3:** Hyperparameter search for CAL weights.

As shown in Figure 4, the complexity and heterogeneity of our image dataset present challenges for accurate segmentation. This figure compares the segmentation results of the standalone Swin Transformer with our proposed LoGSAGE model, which shows improved nuclei delineation in regions with high cellularity, which is characteristic of tumor organization.

## 4. CONCLUSION

This study utilized LoGSAGE model for segmentation as the foundational step in our computational pipeline for profiling the TME. By integrating curvature into the loss function, employing an innovative model architecture, and applying a LoG filter to generate saliency maps, we enhanced the model's sensitivity to segmented nuclei. LoGSAGE achieved a Dice score of 94.92% and a PQ score of 81%, demonstrating its high segmentation accuracy and precision in nuclei detection. Although the addition of CAL might improve the SOTA performance in Table 1, this improvement will likely be minor per the ablation studies of Tables 2-3. Our future direction will be to extend this technique to multispectral images for more robust cellular profiling with the TME.

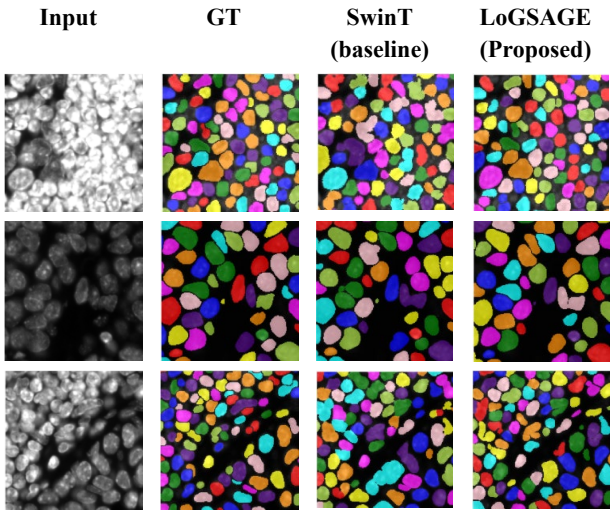


**Fig. 4:** LoGSAGE has better qualitative results as compared to the baseline Swin Transformer.

## 5. ACKNOWLEDGMENT

This research was funded by grants RO1 CA270332 and RO1 CA279408.

## 6. REFERENCES

[1] D. S. Chen and I. Mellman, "Oncology meets immunology: The cancer-immunity cycle," Jul. 25, 2013. doi: 10.1016/j.immuni.2013.07.012.

[2] A. Kirillov *et al.*, "Segment Anything," in *Proceedings of the IEEE International Conference on Computer Vision*, 2023. doi: 10.1109/ICCV51070.2023.00371.

[3] F. Hörst *et al.*, "CellViT: Vision Transformers for Precise Cell Segmentation and Classification," Jun. 2023, [Online]. Available: http://arxiv.org/abs/2306.15350

[4] C. Stringer, T. Wang, M. Michaelos, and M. Pachitariu, "Cellpose: a generalist algorithm for cellular segmentation," *Nat Methods*, vol. 18, no. 1, pp. 100–106, Jan. 2021, doi: 10.1038/s41592-020-01018-x.

[5] M. Weigert and U. Schmidt, "Nuclei Instance Segmentation and Classification in Histopathology Images with Stardist," in *ISBIC 2022 - International Symposium on Biomedical Imaging Challenges, Proceedings*, Institute of Electrical and Electronics Engineers Inc., 2022. doi: 10.1109/ISBIC56247.2022.9854534.

[6] F. Kromp *et al.*, "An annotated fluorescence image dataset for training nuclear segmentation methods," *Sci Data*, vol. 7, no. 1, Dec. 2020, doi: 10.1038/s41597-020-00608-w.

[7] R. Hollandi, N. Moshkov, L. Paavolainen, E. Tasnadi, F. Piccinini, and P. Horvath, "Nucleus segmentation: towards automated solutions," Apr. 01, 2022, *Elsevier Ltd*. doi: 10.1016/j.tcb.2021.12.004.

[8] A. Basu, P. Senapati, M. Deb, R. Rai, and K. G. Dhal, "A survey on recent trends in deep learning for nucleus segmentation from histopathology images," Feb. 01, 2024, *Institute for Ionics*. doi: 10.1007/s12530-023-09491-3.

[9] F. Xing, Y. Xie, H. Su, F. Liu, and L. Yang, "Deep Learning in Microscopy Image Analysis: A Survey," *IEEE Trans Neural Netw Learn Syst*, vol. 29, no. 10, pp. 4550–4568, Oct. 2018, doi: 10.1109/TNNLS.2017.2766168.

[10] Z. Liu *et al.*, "A survey on applications of deep learning in microscopy image analysis," Jul. 01, 2021, *Elsevier Ltd*. doi: 10.1016/j.compbiomed.2021.104523.

[11] O. Ronneberger, P. Fischer, and T. Brox, "U-Net: Convolutional Networks for Biomedical Image Segmentation," May 2015, [Online]. Available: http://arxiv.org/abs/1505.04597

[12] H. Zunair and A. Ben Hamza, "Sharp U-Net: Depthwise convolutional network for biomedical image segmentation," *Comput Biol Med*, vol. 136, Sep. 2021, doi: 10.1016/j.compbiomed.2021.104699.

[13] J. Zhao, Y. J. He, S. Q. Zhao, J. J. Huang, and W. M. Zuo, "AL-Net: Attention Learning Network Based on Multi-Task Learning for Cervical Nucleus Segmentation," *IEEE J Biomed Health Inform*, vol. 26, no. 6, pp. 2693–2702, Jun. 2022, doi: 10.1109/JBHI.2021.3136568.

[14] S. Graham *et al.*, "HoVer-Net: Simultaneous Segmentation and Classification of Nuclei in Multi-Tissue Histology Images," Dec. 2018, [Online]. Available: http://arxiv.org/abs/1812.06499

[15] R. Karimzadeh, E. Fatemizadeh, and H. Arabi, "A novel shape-based loss function for machine learning-based seminal organ segmentation in medical imaging."

[16] Y. Xue *et al.*, "Shape-Aware Organ Segmentation by Predicting Signed Distance Maps," Dec. 2019, [Online]. Available: http://arxiv.org/abs/1912.03849

[17] D. Karimi and S. E. Salcudean, "Reducing the Hausdorff Distance in Medical Image Segmentation with Convolutional Neural Networks," *IEEE Trans Med Imaging*, vol. 39, no. 2, pp. 499–513, Feb. 2020, doi: 10.1109/TMI.2019.2930068.

[18] G. Winkelmaier and B. Parvin, "An enhanced loss function simplifies the deep learning model for characterizing the 3D organoid models," *Bioinformatics*, vol. 37, no. 18, pp. 3084–3085, Sep. 2021, doi: 10.1093/bioinformatics/btab120.

[19] M. Y. Lee *et al.*, "CellSeg: a robust, pre-trained nucleus segmentation and pixel quantification software for highly multiplexed fluorescence images," *BMC Bioinformatics*, vol. 23, no. 1, Dec. 2022, doi: 10.1186/s12859-022-04570-9.

[20] Y. Lin, Z. Wang, D. Zhang, K. T. Cheng, and H. Chen, "BoNuS: Boundary Mining for Nuclei Segmentation with Partial Point Labels," *IEEE Trans Med Imaging*, 2024, doi: 10.1109/TMI.2024.3355068.

[21] Y. Yeganeh, A. Farshad, P. Weinberger, S. A. Ahmadi, E. Adeli, and N. Navab, "Transformers Pay Attention to Convolutions Leveraging Emerging Properties of ViTs by Dual Attention-Image Network," in *Proceedings - 2023 IEEE/CVF International Conference on Computer Vision Workshops, ICCVW 2023*, 2023. doi: 10.1109/ICCVW60793.2023.00244.

[22] M. Caron *et al.*, "Emerging Properties in Self-Supervised Vision Transformers," in *Proceedings of the IEEE International Conference on Computer Vision*, 2021. doi: 10.1109/ICCV48922.2021.00951.

[23] Z. Liu *et al.*, "Swin Transformer: Hierarchical Vision Transformer using Shifted Windows," in *Proceedings of the IEEE International Conference on Computer Vision*, 2021. doi: 10.1109/ICCV48922.2021.00986.

[24] S. Shabani, M. Sohaib, S. A. Mohammed, and B. Parvin, "Multi-Aperture Fusion of Transformer-Convolutional Network (MFTC-Net) for 3D Medical Image Segmentation and Visualization," in *Accepted as a Workshop Paper at T4V@CVPR2024*, 2024.

[25] M. Sohaib, S. Shabani, S. A. Mohammed, and B. Parvin, "3D-Organoid-SwinNet: High-content profiling of 3D organoids," *IEEE J Biomed Health Inform*, 2024, doi: 10.1109/JBHI.2024.3511422.

[26] A. Lee, Z. Jiang, L. Zhu, and W. Ladiges, "QuPath. A new digital imaging tool for geropathology," *Aging Pathobiol Ther*, vol. 2, no. 2, pp. 114–116, Jun. 2020, doi: 10.31491/APT.2020.06.024.